Subdomain cryo-EM structure of nodaviral replication protein A crown complex provides mechanistic insights into RNA genome replication

Nuruddin Unchwaniwala[a,b,c,1], Hong Zhan[a,b,c,1], Janice Pennington[b,c], Mark Horswill[a,b,c], Johan A. den Boon[a,b,c], and Paul Ahlquist[a,b,c,d,2]

[a]John and Jeanne Rowe Center for Research in Virology, Morgridge Institute for Research, Madison, WI 53715; [b]Institute for Molecular Virology, University of Wisconsin–Madison, Madison, WI 53706; [c]McArdle Laboratory for Cancer Research, University of Wisconsin–Madison, Madison, WI 53706; and [d]Howard Hughes Medical Institute, University of Wisconsin–Madison, Madison, WI 53706

Contributed by Paul Ahlquist, June 9, 2020 (sent for review April 2, 2020; reviewed by Ralf Bartenschlager and Richard J. Kuhn)

For positive-strand RNA [(+)RNA] viruses, the major target for antiviral therapies is genomic RNA replication, which occurs at poorly understood membrane-bound viral RNA replication complexes. Recent cryoelectron microscopy (cryo-EM) of nodavirus RNA replication complexes revealed that the viral double-stranded RNA replication template is coiled inside a 30- to 90-nm invagination of the outer mitochondrial membrane, whose necked aperture to the cytoplasm is gated by a 12-fold symmetric, 35-nm diameter "crown" complex that contains multifunctional viral RNA replication protein A. Here we report optimizing cryo-EM tomography and image processing to improve crown resolution from 33 to 8.5 Å. This resolves the crown into 12 distinct vertical segments, each with 3 major subdomains: A membrane-connected basal lobe and an apical lobe that together comprise the ∼19-nm-diameter central turret, and a leg emerging from the basal lobe that connects to the membrane at ∼35-nm diameter. Despite widely varying replication vesicle diameters, the resulting two rings of membrane interaction sites constrain the vesicle neck to a highly uniform shape. Labeling protein A with a His-tag that binds 5-nm Ni-nanogold allowed cryo-EM tomography mapping of the C terminus of protein A to the apical lobe, which correlates well with the predicted structure of the C-proximal polymerase domain of protein A. These and other results indicate that the crown contains 12 copies of protein A arranged basally to apically in an N-to-C orientation. Moreover, the apical polymerase localization has significant mechanistic implications for template RNA recruitment and (−) and (+)RNA synthesis.

positive-strand RNA virus | replication complexes | cryotomography | replication crown | nodavirus

Positive-strand [(+)RNA] viruses contain messenger-sense single-stranded RNA and replicate their genomes in the cytoplasm of infected cells without any DNA intermediates. Such (+)RNA virus genome replication always occurs in complexes associated with host intracellular membranes that have undergone striking, virus-induced rearrangements. Numerous (+)RNA viruses, including the human and animal alphaviruses, the much larger alphavirus-like superfamily, many flaviviruses, nodaviruses, and other viruses, replicate their genomes in 30- to 120-nm "spherules," which are spherical invaginations of host membranes whose site varies with the particular virus (1, 2). Moreover, some coronaviruses produce similar spherules that appear spatially and temporally linked with the double membrane vesicles more commonly associated with coronavirus RNA replication (3). Such RNA replication complexes concentrate the replication factors and templates, orchestrate the successive steps of (−) and (+) RNA synthesis, and sequester double-stranded RNA (dsRNA) and uncapped RNA replication intermediates from innate immune sensing. The central effectors of these processes are nonstructural viral genome replication proteins that target and remodel membranes, recruit additional viral and cellular proteins and viral RNA templates, and provide the enzymatic functions for viral RNA synthesis and often 5′ m^7G capping.

Classic electron tomography has greatly illuminated the dramatic membrane rearrangements associated with such (+)RNA virus replication complexes (4–7). However, due to multiple limitations of traditional electron microscopy (EM) sample preparation and visualization by heavy metal staining, such studies lack information on the organization of viral proteins and RNAs at these sites. At another extreme, multiple (+)RNA virus replication protein structures have been solved to atomic resolution by X-ray crystallography and single-particle cryoelectron microscopy (cryo-EM) of purified proteins (8–17). Although these structures provide critical insights into (+)RNA virus genome replication mechanisms, such studies generally also lack information on the organization of the relevant proteins within native, membrane-bound RNA replication complexes.

Significance

Positive-strand RNA [(+)RNA] viruses constitute the largest genetic class of viruses and include many high-impact pathogens, such as SARS–CoV-2 (COVID-19 pandemic coronavirus), MERS CoV, Zika, chikungunya, dengue, and hepatitis C viruses. (+)RNA virus genome replication invariably occurs on virus-induced, membrane-bound organelles called RNA replication complexes, an attractive potential target for broadly active antivirals. To better understand, control and beneficially employ (+)RNA viruses, urgent needs exist to define RNA replication complex structure and function at a molecular level. This study uses cryoelectron microscopy and complementary approaches to provide previously inaccessible native, near atomic-resolution views of the well-characterized nodavirus RNA replication complex, advancing fundamental understanding of (+)RNA virus genome replication complex structure, organization, stability, and function.

Author contributions: N.U., H.Z., and P.A. designed research; N.U., H.Z., and J.P. performed research; M.H. and J.A.d.B. contributed new reagents/analytic tools; N.U., H.Z., J.P., M.H., J.A.d.B., and P.A. analyzed data; and N.U., H.Z., and P.A. wrote the paper.

Reviewers: R.B., University of Heidelberg; and R.J.K., Purdue Institute of Inflammation, Immunology, and Infectious Disease.

The authors declare no competing interest.

Data deposition: An electron density map of the nodaviral replication protein A crown complex has been deposited in the EMDataBank, https://www.ebi.ac.uk/pdbe/emdb/ (accession no. EMD-22129).

[1]N.U. and H.Z. contributed equally to this work.

[2]To whom correspondence may be addressed. Email: ahlquist@wisc.edu.

This article contains supporting information online at https://www.pnas.org/lookup/suppl/doi:10.1073/pnas.2006165117/-/DCSupplemental.

First published July 20, 2020.

To bridge this gap, we turned to high-resolution cryoelectron tomography (cryo-ET), which can preserve the native structure of (+)RNA virus replication complexes and reveal not only membrane structure but also the structure and organization of viral replication proteins and RNA within the replication complex. Perhaps the best-studied current model for such studies is the nodavirus flock house virus (FHV). FHV is a simple (+)RNA virus that expresses three RNAs (genomic RNA1 and RNA2 and subgenomic RNA3) and four proteins (protein A, capsid, B1, and B2) (Fig. 1) (18). Protein A (998 aa), the only viral protein required for spherule formation and RNA replication (19), has two known enzymatic domains: An N-proximal RNA-capping domain and a C-proximal RNA-dependent RNA polymerase (RdRp). Protein A also has two membrane-association domains: A well-established N-terminal transmembrane domain and, in keeping with significant membrane interaction after deletion of this transmembrane segment, a predicted membrane-interaction region within the Iceberg domain (Fig. 1) (20–23). Finally, various distinct multimerization regions within the capping, Iceberg, and RdRp domains are required for protein A self-interaction and function in RNA replication (24).

FHV forms its spherule RNA replication complexes as 30- to 90-nm invaginations of outer mitochondrial membranes (OMMs) (5, 25, 26). Using this FHV model system, our group recently demonstrated that mitochondria isolated from FHV-infected *Drosophila* cells maintain intact, highly active RNA replication complexes that, when imaged by cryo-ET, yielded novel structural insights into the organization and interactions of RNA, protein, and membranes in the replication complex (25). Among other findings, these studies revealed a striking, 12-fold symmetric, protein A-containing "crown" complex above the cytoplasmic side of the spherule neck, and employed preliminary subtomogram averaging to image the crown structure to an initial resolution of 33 Å (25).

In this study, we combined multiple advances in sample preparation, cryo-ET image acquisition, image processing, and subtomogram averaging to improve the crown resolution by nearly fourfold to 8.45 Å. The results reveal the crown's distinct architecture, with each of the 12 distinct crown segments bearing three subdomains, two membrane contacts, and multiple crown-building interactions with flanking segments. An engineered tag in an RNA replication-competent chimeric protein A was used to map the C-proximal RdRp domain to the apex of the crown. The results indicate that the crown is largely—if not completely—composed of 12 copies of viral protein A, illuminate protein A–membrane and protein A–protein A interactions that stabilize the spherules, and reveal that each protein A is generally oriented in the crown from basal N to apical C domains, a positioning with distinct mechanistic implications for RNA template recruitment, (−)RNA synthesis, and (+)RNA synthesis and capping. Overall, these findings provide strong foundations and specific hypotheses for further experiments, and substantial mechanistic implications for broader understanding of (+)RNA virus genome replication.

Results

Optimized Data Acquisition and Processing Retain High-Resolution Information in Cryotomograms. Samples for cryo-ET were generated by infecting *Drosophila* S2 cells with purified FHV followed by mitochondrial isolation and plunge-freezing. The comparatively thick nature (>200 nm) of mitochondrial samples on cryogrids reduces the signal-to-noise ratio in tomograms (27, 28). To minimize such sample thickness effects and increase the high-resolution information in the cryotomograms, we employed multiple emerging practices for improved cryo-ET data collection and processing, including motion correction via dose fractionation (29), use of a dose-symmetric tilt scheme (30), lower 3.5-μm defocus, and 3D contrast transfer function correction (31).

Fig. 2 *A* and *B* shows a sample section of a reconstructed tomogram displaying numerous spherule vesicles, contiguous with the OMM, containing densely coiled fibrils and surmounted by crowns (Fig. 2 *A*, *C*, and *E*). In a distinct location of the same tomogram, crown structures are visible from the top view (Fig. 2 *B*, *D*, and *F*). Even without subtomogram averaging, many key structural features, such as the central turret, regularly spaced projections outwards from the central turret, and central densities within the turret are evident.

Subtomogram Averaging Reveals Underlying Crown Structural Domains. A total of 4,640 crowns from 59 tomograms were used for subtomogram averaging. First, 1,608 manually picked crowns and the IMOD/PEET software (32, 33) were used to generate a 24-Å resolution subtomogram-averaged crown template. This template was used to identify more crowns in the tomograms by the automated template-matching feature in emClarity (34) (Movie S1), increasing the total crown images by nearly threefold to 4,640. In addition to increasing the yield of crown images, such automated selection overcomes potential user bias in particle selection, identifies crowns in multiple orientations, registers crown orientation without user input, and works with lower defocus (low-contrast, higher-resolution) tomograms.

Further subtomogram averaging was performed using the emClarity software suite (34). The crown has 12-fold symmetry (c12) (25), which is apparent in top views of individual crowns from the regularly spaced outward projections from the central turret (Fig. 2*D*), particularly when multiple *z*-series elevations are examined to better view the full circumference (Movie S2). Initial subtomogram averaging without imposing any symmetry generated a 10.37-Å crown structure displaying c12 symmetry (*SI Appendix*, Fig. S2 *A*–*C*). Accordingly, to further improve the resolution, we imposed c12 symmetry during the iterative subtomogram-averaging process, yielding a crown image with a resolution of 8.45 Å, as determined by Fourier shell correlation (*SI Appendix*, Fig. S2*D*). Neither our visual inspection nor preliminary computational subclassification has revealed structures lacking 12-fold symmetry. Hence, incomplete crowns, if present, do not represent a significant structural class.

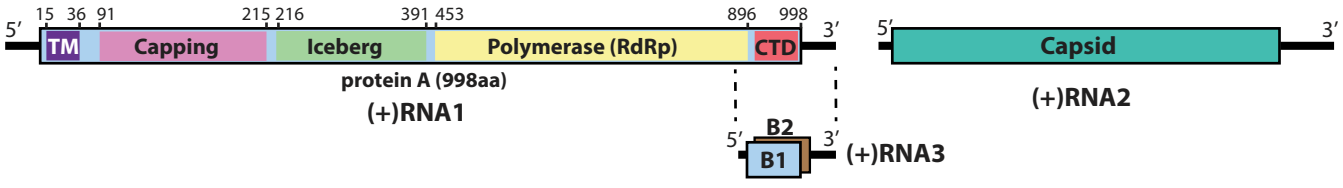

Fig. 1. Genome organization and protein ORFs of FHV. The bipartite FHV genome, (+)RNA1 and (+)RNA2, express protein A and capsid protein, respectively. Protein A is the master FHV RNA replication protein that is involved in various functions such as membrane association (transmembrane domain and a possible membrane-interacting domain in the Iceberg region), replication complex formation, RNA 5′ capping, and RdRp enzymatic activities. The various functional domains of protein A are highlighted in the ORF and their amino acid coordinates are marked above the ORF. Note that both the indicated core RNA-capping domain and the adjacent Iceberg domain appear to contribute to RNA-capping functions (20). Protein A replicates the viral RNAs to form minus-sense products, likely as dsRNA. During minus-strand synthesis, a FHV RNA1 3′ end coterminal (−)RNA3 is synthesized, which in turn replicates to make the (+)RNA3. RNA3 codes for the B1 and B2 proteins. B1 is a preferentially nuclear protein with unknown function, whereas B2 is a well-established RNAi suppressor.

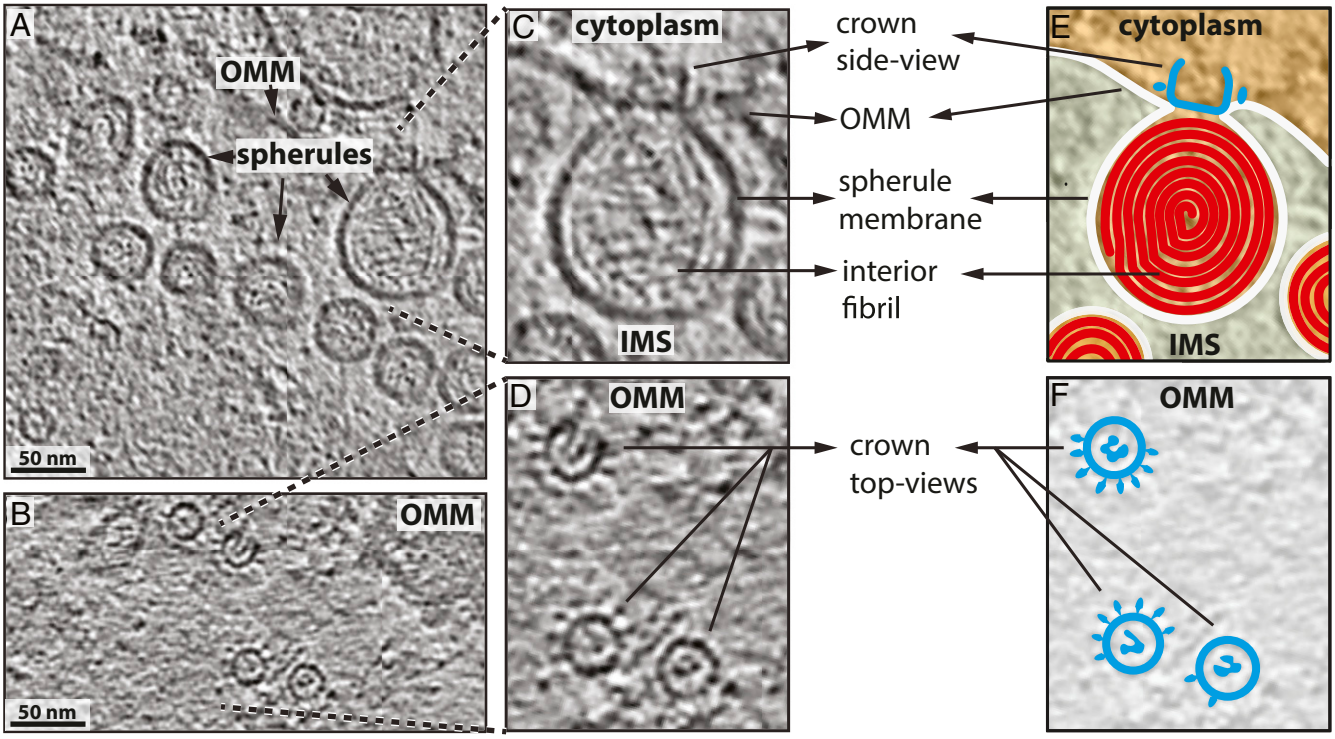

Fig. 2. Improved cryo-ET procedures to visualize FHV replication complexes at the mitochondria. (*A*) Section of the reconstructed tomogram showing the side view of FHV replication complexes. Various spherules and the OMM are highlighted with black arrowheads. (*B*) Section of the reconstructed tomogram showing the top view of the OMM with FHV replication complex crowns. (*C* and *D*) *Insets* of *A* and *B* showing a zoomed-in view of a single spherule and three top views of the crown, respectively. (*E*) False-color representation of *C* highlighting the various densities and subcellular regions at the replication complex. Blue, crown side view; white, OMM; red, densely coiled internal fibril; translucent orange, cytoplasm; and translucent green, mitochondrial intermembrane space (IMS). (*F*) False-color representation of *D* highlighting the top view of the OMM (translucent white), and the crowns (blue).

Fig. 3 and Movie S3 display how this approximately fourfold increase in resolution from prior imaging (25) reveals that the crown is composed of three major subdomains. The ~19-nm-diameter central turret is composed of a basal domain or lobe connected at its foundation to the OMM (Fig. 3 *A*, *Inset*, and Fig. 3*B*) and supporting an apical lobe poised directly above. The apical lobe is ~6-nm tall and ~4.5-nm wide, whereas the basal lobe is ~7-nm tall and 4.5-nm wide. Additionally, the left side of the basal lobe's exterior face anchors a leg domain that extends radially outward to ~7 nm from the basal lobe before bending down to form a second connection with the OMM at a diameter of ~35 nm (Fig. 3 *C* and *E*). Previous lesser-resolution imaging of the crown revealed the lower portion of this leg as a projection slightly angled toward the central turret, although the connection with the basal lobe was not resolved (Movie S3) (25). Notably, the improved imaging used here makes this connection to the basal lobe visible even in the primary tomograms, prior to subtomogram averaging (Fig. 2*D*).

In addition to the vertical connection of the basal and apical lobes, horizontal interactions connect each pair of adjacent apical domains and each pair of adjacent basal domains to form the crown ring (Fig. 3 *A*, *Inset*, and Fig. 3*D*). Although clearly evident, these circumferential interactions are less substantial than the vertical basal-to-apical domain connections and disappear more quickly if the electron-density threshold is increased to selectively display the highest-density regions (Movie S4). Potential relation of these lateral interactions to multimerization interactions mapped within protein A (24) is considered in *Discussion*. Progressively sectioning the electron-density map through successive top- and side-view planes shows internal-density variations indicative of protein secondary structure and further illustrates the distinct natures of the apical, basal, and leg domains (Fig. 4 and Movie S5).

Crown Constrains Shape of Membrane Vesicle Neck. Although the diameters of the underlying replication vesicles varied over several classes from ~30 to 90 nm (Fig. 2*A*) (25), subtomogram averaging over the 4,640 crowns used also closely reinforced the structure of the vesicle neck adjoining the crown (Fig. 3 *B* and *C*). Thus, unlike the varied curvature of the vesicle bodies, the membrane shape and curvature at the neck is highly uniform. This close alignment of the membrane neck structure with the crown implies that the crown does not simply passively reside on top of the vesicle neck. Rather, like tying the neck of a pressurized balloon, strong crown–membrane interactions appear to play a primary role in forming and stabilizing the neck, thus preventing the high-energy replication vesicle from bursting open due to the electrostatic repulsion of the closely packed viral dsRNA within.

Particularly with the improved overall resolution, the higher electron-density protein crown (Fig. 3*A*) and the neighboring, lower electron-density lipid bilayer could be distinguished by adjusting the electron-density threshold for imaging (Fig. 3*C*). Fig. 3*B* shows a cross-section with the higher-density protein crown (opaque blue) encased within a lower-density threshold image (transparent white), in which the major additional volume is derived from the membrane neck of the replication vesicle invaginated from the flanking OMM. Of note, the polar head groups on each side of the lipid bilayer are more electron dense than the intervening fatty acyl chains, causing the membrane to appear as two parallel layers ~3 nm apart (35). Interestingly, in the region between the two membrane contacts of the crown, these two headgroup layers appear to approach each other more closely or be bridged by an unknown density (Fig. 3*B*, asterisks). Possible reasons for this effect are considered in *Discussion*.

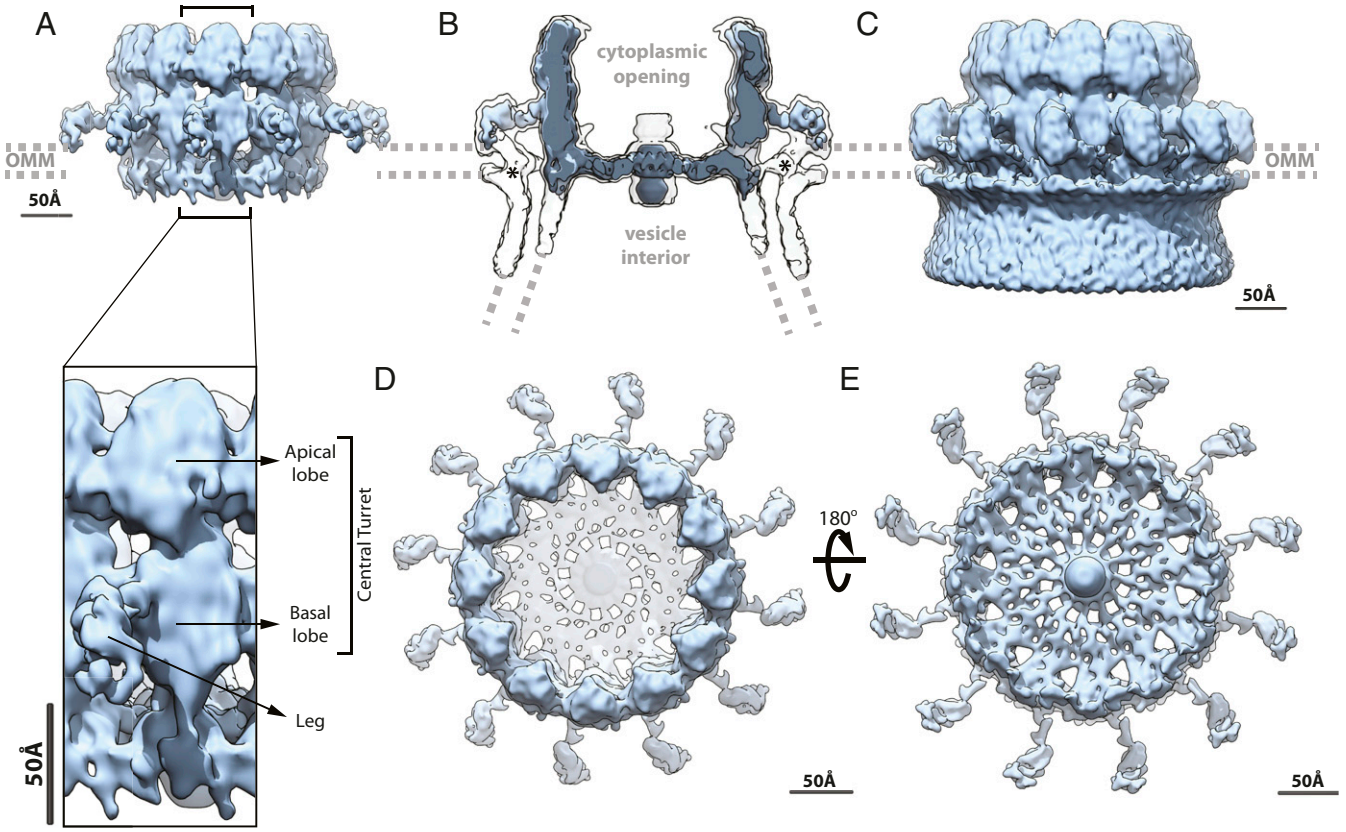

Fig. 3. Subtomogram averaging of the crown structure reveals important new structural details. (*A*) High-density threshold (contour level = 4.2) side view of the crown. The dotted gray line through the *A*, *B*, and *C* map the OMM for point of reference. (*Inset*) Region in *A* marking the three structurally distinct regions in the crown: apical lobe, basal lobe, and leg. (*B*) Cross-section view of the low-density threshold crown (from *C*) as a transparent white shell encasing the high-density crown (from *A*) in blue. Asterisks indicate unusual densities bridging between denser head group regions of the lipid bilayer, and the dashed lines below the crown depict the continuation of the reshaped OMM into the body of the spherule RNA replication vesicle. (*C*) Low-density threshold (contour level = 2) side view of the crown show the additional density contributions made by the membrane. (*D*) Top view of the high-density threshold crown highlights the 12-fold symmetry of the crown complex. (*E*) Bottom view of the high-density threshold crown.

Inside the central turret, near the level of the OMM, the crown appears partly or largely closed by a mesh or floor of electron density (Fig. 3 *B*, *D*, and *E*). Similar local densities at this level are also evident in side views of individual crowns prior to subtomogram averaging (Fig. 2 *C* and *E*). In the averaged structure, the center of this floor is occupied by a more elongated cylindrical density (Fig. 3*B*) potentially related to the external filaments that often proceed from crowns tens of nanometers into the extra mitochondrial space, and may represent nascent progeny RNAs (25). Intriguingly, top views of individual crowns (Fig. 2 *D* and *F*) frequently show asymmetric densities within the central turret that, through subtomogram averaging, may contribute significantly to the "floor" density in Fig. 3*B*. Due to their marked heterogeneity, efforts toward asymmetric reconstruction of these central densities have not yet yielded an informative local subtomogram average. It also is presently uncertain whether, in addition to any protein components, a portion of the floor density might be contributed by locally constrained segments of the internal filaments that occupy the replication vesicle and are thought to represent viral genomic dsRNA (25) (Fig. 2 *A* and *C*).

Protein A C-Terminal End Is Exposed at FHV Replication Compartment. Protein A is the only viral protein required for nodavirus RNA replication complex formation and a major component of the crown complex (19, 22, 24, 25). Moreover, protein A is a highly self-multimerizing, OMM-associated protein that supports RNA synthesis and RNA-capping enzymatic activities during the viral life cycle (19, 22–24) (Fig. 1).

To better understand the organization and function of protein A in the crown, we sought to further map protein A's position, orientation, and stoichiometry with the aid of suitable tags. Although at many positions in protein A even short epitope tag insertions abolish RNA replication, we found that the C terminus accepted a 16-aa GFP11 peptide tag while retaining 80% of WT RNA replication activity *in cis* (Fig. 5 *A* and *B*). As part of the split-GFP system (36), this tag can be complemented for fluorescence by its binding partner GFP1-10. Moreover, C-terminal tagging was advantageous because the C terminus is adjacent to the protein A RdRp domain, a domain of high interest (Fig. 1). The biologically active protein A–GFP11 fusion was expressed from a DNA plasmid that transcribes FHV RNA1 from the baculovirus immediate early (IE1) promoter in transfected *Drosophila* S2 cells, launching replication of genomic RNA1 and its product, subgenomic RNA3 (Fig. 5*B*). Expression of RNA1-derived subgenomic RNA3 and its encoded B2 RNAi suppressor protein were maintained to avoid otherwise potent RNAi knockdown of replication (37). However, in the relevant plasmid, pRNA1-GFP11-ΔB1, translation of RNA3's other product, protein B1, was knocked out by a M897L change at the B1 initiating methionine codon (Fig. 5*A*). This was done since the B1 ORF is in-frame with the C-terminal 102 aa of protein A, so that B1 expression would have yielded a second GFP11-tagged protein, complicating localization of GFP11-tagged protein A. Prior results showed that knocking out B1 expression does not inhibit FHV infection and RNA replication in the *Drosophila* DL-1 cell (38).

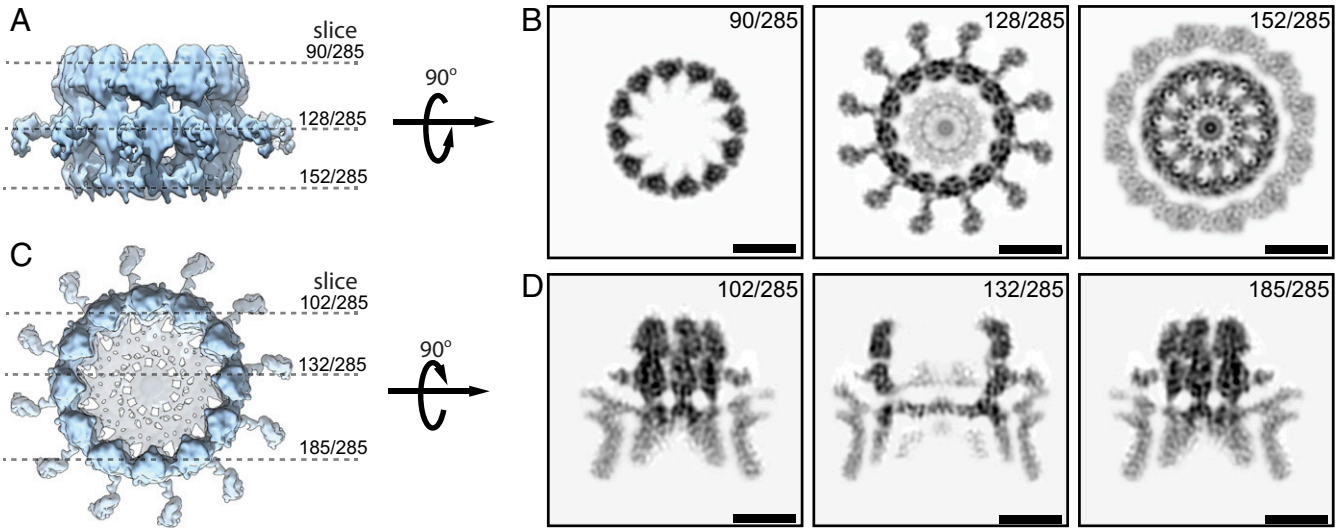

Fig. 4. Two-dimensional slices of the crown electron-density map display the higher-resolution substructure. (*A* and *B*) High-density threshold side view of the crown with dotted lines representing the slices shown in *B* after 90° rotation. (*C* and *D*) High-density threshold top-view of the crown with dotted lines representing the slices shown in *D* after 90° rotation. (Scale bars in *B* and *D*, 10 nm.)

To assess if the C terminus of protein A is exposed at FHV RNA replication sites on mitochondria, we cotransfected *Drosophila* S2 cells with a plasmid expressing GFP1-10 together with either pRNA1-WT, expressing WT RNA1 (Fig. 5 *C*, *Upper*), or pRNA1-GFP11-ΔB1 (Fig. 5 *C*, *Lower*). Fluorescence microscopy showed that protein A-GFP11, and not WT protein A, successfully complemented GFP1-10, and that the resulting GFP fluorescence colocalized (Pearson correlation coefficient [PCC] = 0.88 ± 0.1, 88 cells analyzed), as expected with protein A immunofluorescence (Fig. 5*C*). To test whether GFP1-10 complementation could occur with OMM-associated protein A on preformed replication complexes, we used pRNA1-GFP11-ΔB1 to generate infectious FHV virions that express the protein A-GFP11 fusion upon infection and can complement GFP1-10 in vivo (Movie S6). We isolated mitochondria from S2 cells lacking GFP1-10 and infected with WT FHV or FHV-GFP11-ΔB1 virions. Samples of these mitochondria were or were not supplemented with maltose binding protein (MBP)-GFP1-10 purified from *Escherichia coli* and GFP fluorescence was measured over time. As seen in Fig. 5*D*, mitochondria from RNA1-GFP11-ΔB1 FHV-infected cells complemented with GFP1-10, but not the negative controls lacking GFP11 or GFP1-10, showed growing GFP fluorescence over time. Together, these results show that mitochondria in FHV-infected cells bear large amounts of protein A whose C terminus is exposed to the cytoplasm and accessible to the GFP1-10 protein, as opposed to being occluded behind a barrier of membrane or other protein domains.

Site-Specific Nanogold-Labeling Maps Protein A C Terminus to Crown Apex. To identify the position of the exposed C-terminal end of protein A at the crown, we combined Ni-NTA-nanogold–labeling and EM. Such Ni-NTA-nanogold labeling has successfully mapped the position of hexahistidine (His)-tagged protein domains within varied protein complexes, in part since gold's high electron-density renders tagged complexes easy to identify for use in subtomogram averaging (40–43). Ni-NTA-nanogold also provides relatively precise localization of His tags since, as no additional proteins are involved, the distance from the gold particle to the tag is only ∼1.8 nm.

Accordingly, we generated a pRNA1-His-ΔB1 expression plasmid by substituting 4 aa within the GFP11 tag of protein A-GFP11 with histidine residues to yield a His-tag (Fig. 5*A*). The resulting RNA1-His-ΔB1 retained 58% of WT RNA replication activity in transfected S2 cells (Fig. 5*B*). Using pRNA1-His-ΔB1, we generated infectious FHV-His-ΔB1 virions that expresses the protein A His-tag fusion upon infection of S2 cells and confirmed the presence of the His-tag by immunofluorescence. As seen in Fig. 5*E*, S2 cells infected with FHV-His-ΔB1 produce colocalizing signals with antibodies against protein A and the His-tag (PCC = 0.94 ± 0.05, 100 cells analyzed), while WT FHV-infected S2 cells stain with antibodies against protein A, but not against the His-tag.

To nanogold-label the His-tag on protein A at the crown, we infected S2 cells with FHV-His-ΔB1 or WT FHV virions and isolated mitochondria 16 h postinfection. The mitochondria were incubated with 5-nm Ni-NTA-nanogold particles at 4 °C for 1 h, and then were plunge-frozen (Fig. 6*A*). Cryo-ET imaging shows the high-specificity, high-density nanogold labeling of mitochondria from cells expressing protein A-His, but not WT protein A (Fig. 6*B*). Furthermore, for mitochondria from cells infected with FHV-His-ΔB1 virions, the nanogold labels specifically appear on OMM segments that are decorated with spherules and not at OMM segments without spherules (Movie S7). This confirms that protein A is only detectably present on the OMM at the sites of RNA replication, consistent with our prior immunogold-labeling results using an antibody against protein A (25). Note that in this experiment with intact, unsectioned mitochondria, any protein A that might be present within the replication spherules would not be detected since the OMM and spherule membrane block Ni-NTA-nanogold access to the spherule interior (*Discussion*).

As shown by representative examples in Fig. 6 *B*, *Right Inset* and Fig. 6*C*, individual spherules bearing nanogold labels consistently show labeling above RNA replication vesicle necks (i.e., at the sites of crowns, which were usually directly visible in the tomograms) at ∼15 nm above the surface of the OMM. Combining the 1.8-nm linker distance between the nanogold and His-tag and the ∼14-nm height of the central turret from the membrane roughly positions the nanogold at the apex of the crown.

To confirm this, we collected a higher resolution cryo-ET dataset (representative examples in Fig. 6*C*) and used IMOD/PEET to perform iterative subtomogram averaging on 141 unlabeled crowns alone or in combination with 184 nanogold-labeled crowns from the same tomogram, to control for any variations in crown structure due to sample preparation. When subtomogram averaging the labeled crowns, we found that the highly electron-dense nanogold particles dominated the crown alignment process, leading the program to

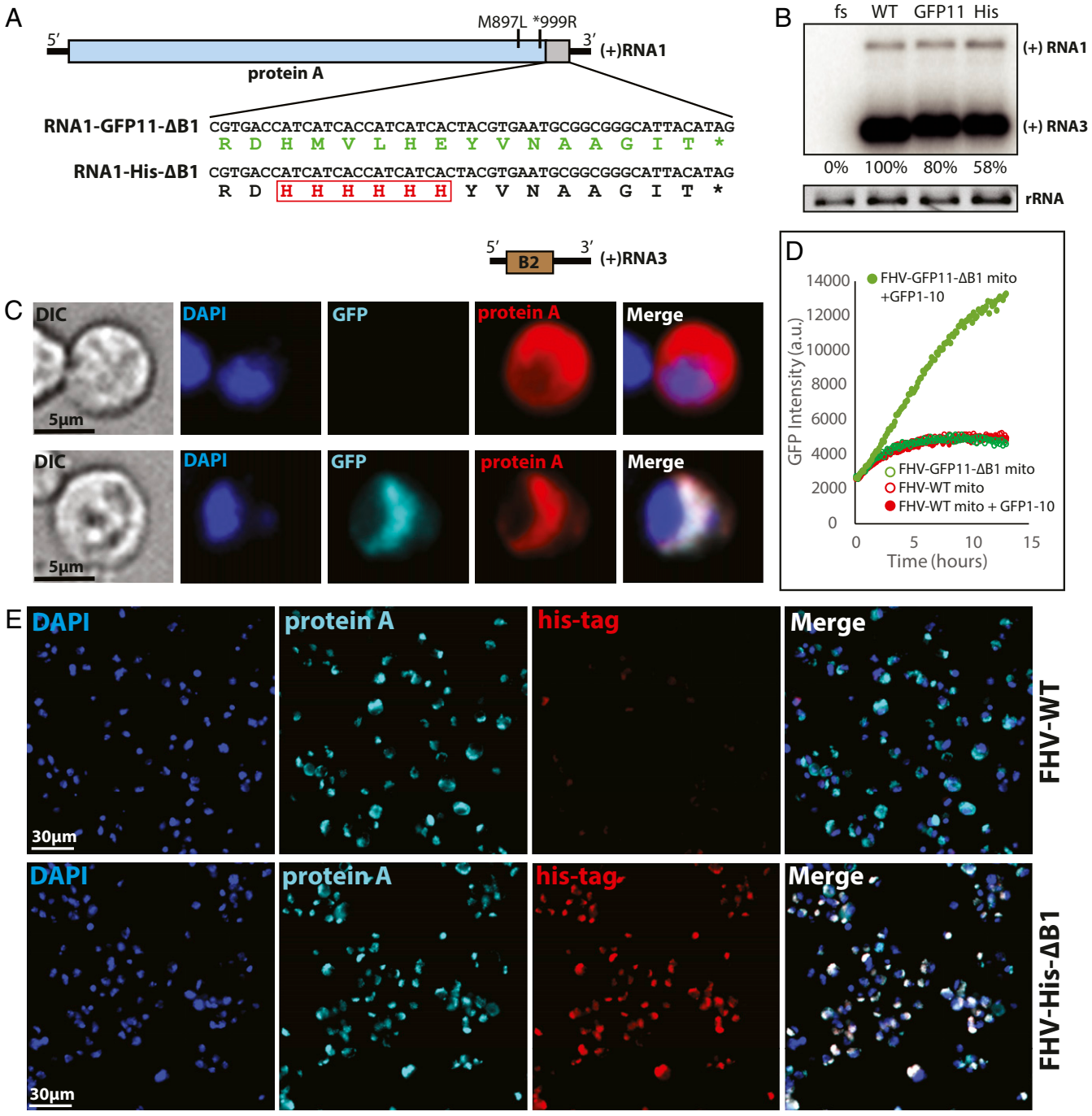

Fig. 5. C terminus of protein A is exposed at the mitochondria in cells replicating FHV. (*A*) RNA1-GFP11-ΔB1 construct incorporates three distinct changes: 1) M897L amino acid change to knock out B1 expression, 2) *999R amino acid change to extend protein A ORF, and 3) C-terminal extension of protein A ORF to express a 16-aa GFP11 sequence (amino acids 1,008 to 1,023). RNA1-His-ΔB1 disrupts the GFP11 sequence to incorporate the His-tag at amino acid positions 1010 to 1015 within protein A. (*B*) Northern blot analysis on RNA isolated from cells transfected with the indicated FHV RNA1 expression plasmids to compare *in cis* RNA replication capacity of the encoded protein A fusions. fs = RNA1fs, GFP11 = RNA1-GFP11-ΔB1, His = RNA1-His-ΔB1, and WT = RNA1-WT. Ribosomal RNA (rRNA) shown as a loading control. RNA1fs is a full-length RNA1 derivative in which an engineered frameshift blocks protein A expression (39). (*C*) Widefield fluorescence microscopy of S2 cells. (*Upper*) Cells transfected with expression plasmids RNA1-WT and GFP1-10 and (*Lower*) cells transfected with RNA1-GFP11- ΔB1 and GFP1-10 plasmids. Immunostained protein A is shown in red and GFP fluorescence shown in cyan. The Merge image includes the three channels to the left. (*D*) In vitro complementation of mitochondria from FHV-WT or FHV-GFP11-ΔB1 infected S2 cells with *E. coli*-purified MBP-GFP1-10 and measurement of GFP fluorescence over time. (*E*) Widefield immunofluorescence analysis of S2 cells infected with FHV-WT or FHV-His-ΔB1. S2 cells costained with antibodies against protein A and His-tag.

orient the labeled complexes with nanogold particles superimposed, but with the protein crowns frequently rotated out of alignment to each other. To avoid this distortion, we used a defined mask to align the labeled complexes solely by reference to the protein densities of the crown, eliminating the influence of the nanogold on alignment. The resulting alignments were then used for subtomogram averaging of the entire complex, including the protein crown and the nanogold, such that the nanogold densities were rotationally averaged around

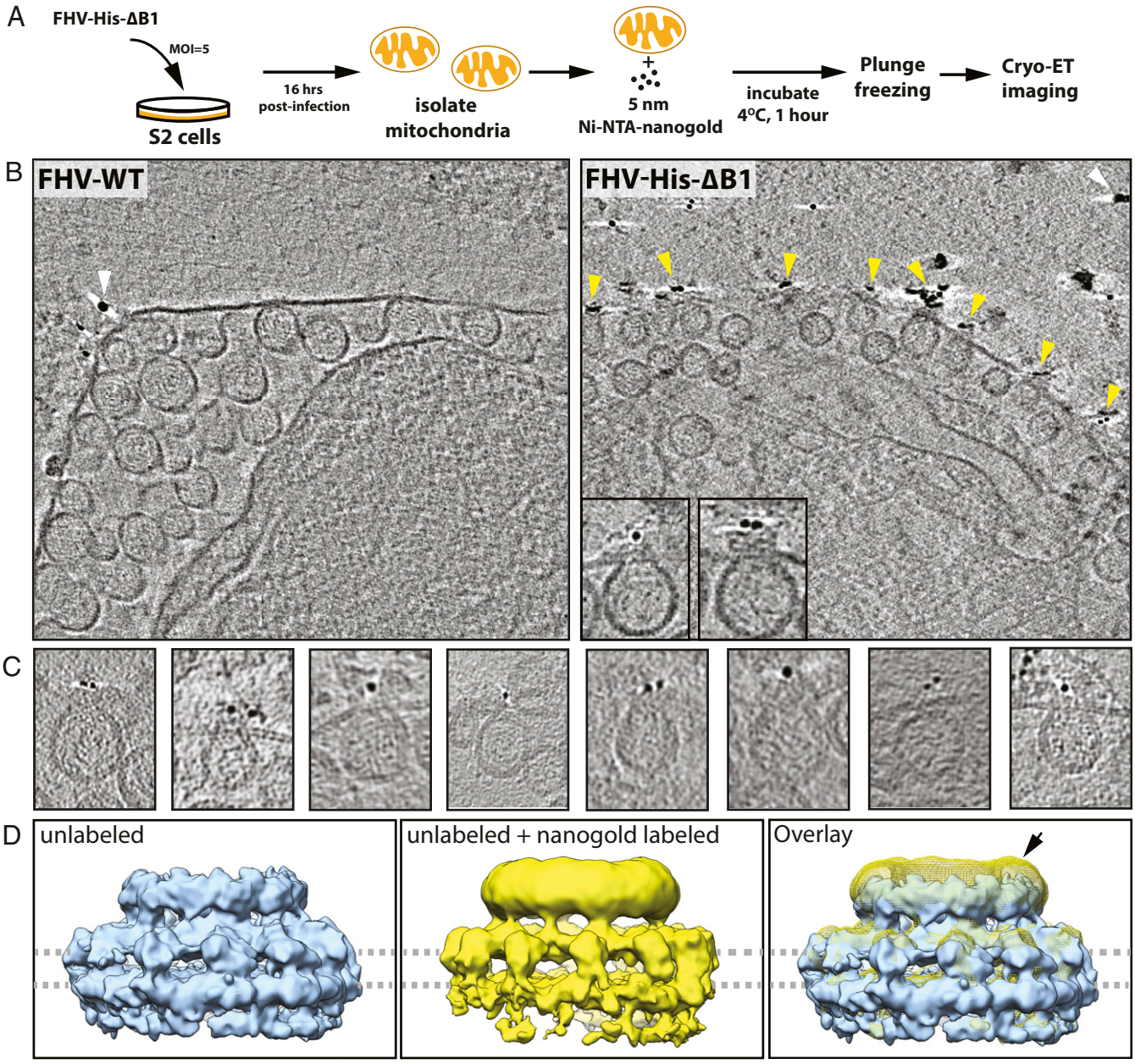

Fig. 6. Site-specific nanogold labeling maps the protein A polymerase domain to the distal lobe of the crown. (*A*) Experimental scheme for infection, isolation, and native labeling of His-tagged protein A with 5-nm Ni-NTA-nanogold for cryo-ET imaging. (*B*) Reconstructed tomograms of mitochondria isolated from FHV-WT (*Left*) or FHV-His-ΔB1 (*Right*) after nanogold-labeling. The white arrowheads indicate 10-nm fiducial gold used for alignment during tomogram reconstruction of both samples. The yellow arrowheads indicate the 5-nm Ni-NTA-nanogold. (*Right Insets*) Two individual spherules showing nanogold-labeling. (*C*) Representative nanogold-labeled subtomograms from a higher resolution cryo-ET dataset. (*D*) Subtomogram averaging of nanogold-labeled and unlabeled crowns. Unlabeled = 141 unlabeled crowns used for averaging. Unlabeled + nanogold labeled = 141 unlabeled crown + 184 gold labeled crowns included in averaging. Overlay = Unlabeled crown in blue overlayed with a mesh view of the unlabeled + nanogold-labeled crown in yellow. The black arrow highlights the major additional densities contributed by the nanogold appearing at the apex of the crown.

the entire crown ring. Comparing the average of the unlabeled crowns (Fig. 6 *D*, *Left*) to the combination of unlabeled and nanogold-labeled (Fig. 6 *D*, *Center*), the averaged additional densities of the nanogold particles appear at the top of the crown, around and above the apical lobe of the central turret (Fig. 6 *D*, *Center* and *Right*). These results indicate that the C terminus of protein A is positioned at or very near the top of the apical lobe.

Apical Lobe EM Density Correlation with Protein A Polymerase Domain. The C terminus of protein A, mapped above to the top of the crown apical lobe, is adjacent to the RdRp domain (Fig. 1). Polymerase domains in (+)RNA viruses are highly structurally conserved despite amino acid sequence divergence (44). To date, there are no available atomic or near-atomic resolution structures for nodaviral protein A or any of its functional domains. Hence, we performed structure prediction on the polymerase domain of FHV protein A (amino acids 453 to 896) using the iTasser software suite (45). On the left side of Fig. 7*A*, the predicted structure of the FHV polymerase (Pol-Pred) is shown with the template entry, NTP entry, and product exit sites indicated and the product exit pore facing the viewer. iTasser predicts that the FHV protein A polymerase domain has high structural similarity to RNA polymerases from the family

Flaviviridae, with the highest similarity to genus Pestiviruses within that family. As also shown in Fig. 7*A* in matching orientation for comparison, the top four structurally similar polymerase domains were from classic swine fever virus (CSFV), bovine viral diarrhea virus (BVDV), Japanese encephalitis virus (JEV), and Zika virus (ZIKV) with 97.8% structurally aligned residues for CSFV to 90.8% for ZIKV.

As shown in Fig. 7*A*, Pol-Pred and viral RdRps in general are wider in the fingers region than at the distal thumb domain. The EM density map of the apical lobe has a wider base that gradually tapers toward the apex (Fig. 3 *A*, *Inset*). Accordingly, the best fit of Pol-Pred into the apical lobe EM-density envelope is clearly with the finger domains at the bottom and the thumb at the top (Fig. 7*B*). Interestingly, this places the C terminus at the top of the apical lobe (see N–C ribbon diagram color gradient in Fig. 7*B*), matching the nanogold results (Fig. 6*D*). Additionally, we utilized the Segger rigid-body docking method (46, 47) to find the best fit of Pol-Pred into the apical lobe by allowing 100 rotations around the three principal axes to locate the highest correlation fits. Consistent with our manual docking results, the top two fits provided by Segger also dock the Pol-Pred with the finger domain at the bottom and the thumb domain at the top of the apical lobe, although the two fits differ by a 180° rotation around the *y* axis (i.e., the vertical axis in the plane of the figure) (Fig. 7*C*). Since the docking scores of these two fits are not dramatically distinguished, the current resolution crown structure does not appear to allow unambiguously predicting the orientation of Pol-Pred around the *y* axis (*SI Appendix*, Fig. S3). Nevertheless, taken together, both the nanogold mapping and these modeling results are consistent with the general N-to-C orientation of protein A from the basal to the apical lobe, positioning the polymerase domain in the apical lobe with its N terminus at the interface between the apical and basal lobes. The mechanistic implications of this polymerase position in the crown for viral genome replication are considered further in *Discussion*.

Discussion

This study combines improved sample preparation, cryo-ET data collection, and image processing to improve the resolution of the nodavirus RNA replication complex crown by nearly fourfold. The resulting 8.45-Å structure reveals that the crown is composed of 12 segments, each with apical, basal, and leg domains and 2 membrane binding sites (Fig. 3 *A*, *Inset* and Fig. *B–D*). Below we discuss the relation of these features to multifunctional viral replication protein A, mapping of protein A's RdRp domain to the apical lobe, and mechanistic implications for sequential RNA replication steps, with potentially wider implications for the many other (+)RNA viruses with similar RNA replication vesicles.

Protein A Forms a Dodecameric Crown Complex. Multiple aspects of our findings imply that the crown (Fig. 3 *A*, *Inset*) is largely or exclusively comprised of 12 copies of protein A. Nanogold-labeling mapped the C terminus of protein A to the top of the crown apical domain (Fig. 6), whose 12-fold repetition shows that the crown contains 12 copies of protein A. Given the ~1.35 g/cm^3 average density of globular proteins (48, 49) and ~20% variation in packing density across proteins (50), protein A (998 aa) is expected to occupy a volume of ~125 to 150 nm^3. This reasonably matches the estimated 150-nm^3 volume of a single crown segment (apical + basal + leg domains) as shown in Fig. 3*A*, particularly since Fig. 7 and Movie S4 show that the Fig. 3*A* electron-density threshold is highly conservative and likely overestimates the actual volume.

The organization of each crown segment with basal and apical lobes and two membrane contact points (Fig. 3 *A* and *B*) also parallels protein A's two enzymatic domains (methyltransferase-guanylyltransferase [MTase-GTase] and RdRp) (Fig. 1) and present understanding of protein A–membrane interaction. Protein A has a mitochondrially targeting transmembrane domain in its N-terminal 36 aa (23) and additional downstream membrane-interaction capability since, after deleting the N-terminal transmembrane domain alone or with flanking sequences out to amino acid 245, 40 to 64% of protein A still fractionates with membranes (23). One possible site for this downstream membrane binding is

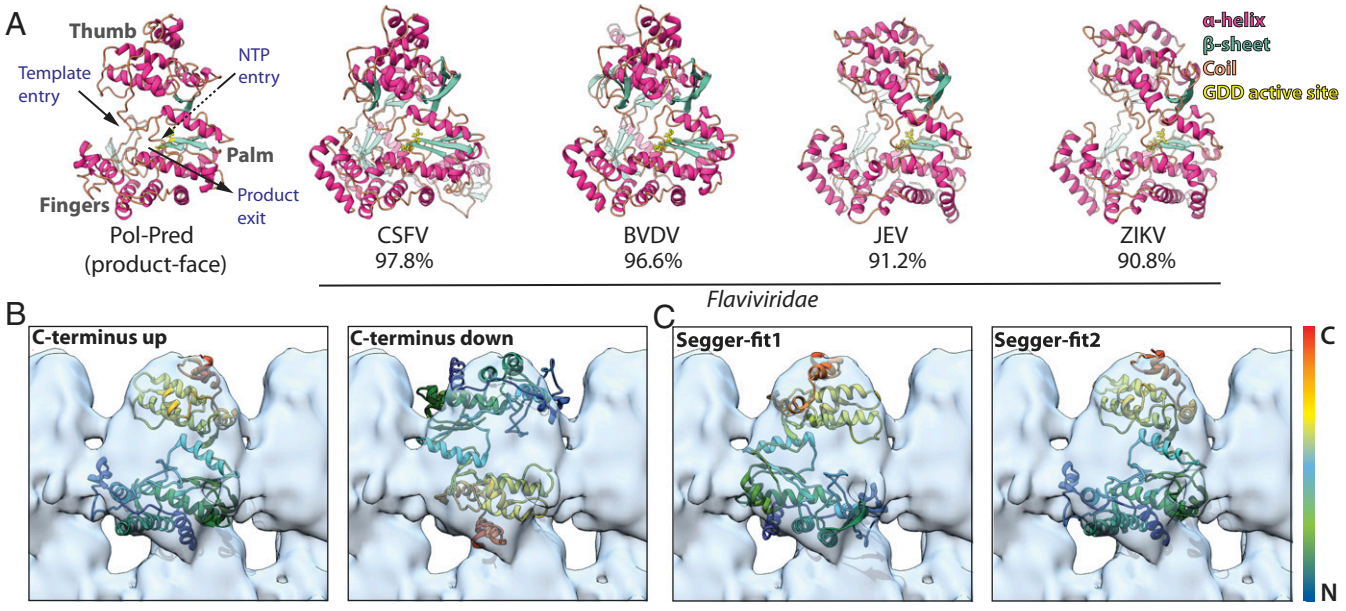

Fig. 7. Protein A polymerase secondary structure prediction and fitting into the EM density map. (*A*) iTasser predicted secondary structure of protein A polymerase domain (Pol-Pred, amino acids 453 to 896) shown to the left with the product-exit face in the front. The top four iTasser structural analogs shown (high to low, left to right) in the same orientation as the FHV-predicted polymerase domains. (*B*) Manual C terminus up and down fit of Pol-Pred into the EM density map. The Pol-Pred structure is rainbow colored from the N to the C terminus going from blue to red. The N-to-C color key is also shown to the right. (*C*) Top two fits (based on correlation score) obtained from fitting Pol-Pred into the segmented apical lobe using the rigid-body docking tool in Segger.

protein A's Iceberg region (amino acids ~216 to 391) (Fig. 1), which shares similarity with membrane-binding Iceberg regions conserved across the alphavirus superfamily (20).

Additionally, the side interactions that join apical to apical and basal to basal lobes to form the crown ring (Fig. 3 *A*, *Inset*) match prior mapping of multiple, independent protein A multimerization domains in the MTase-GTase core, Iceberg, and RdRp regions (24). Within these regions, alanine substitution mutations that inhibit protein A multimerization also inhibit RNA replication. The findings implied that multiple interactions zipper two or more copies of protein A together for at least some required functions, but the nature and stoichiometry of the complex was unknown. The results presented here show that 12 copies of protein A reside in the crown like staves in a barrel, with the multimerizing interactions joining the segments like hoops on a barrel.

Protein A Is Oriented N-to-C from Crown Basal to Apical Regions. The general orientation of protein A in the crown is defined by our nanogold mapping of the C terminus to the top of the crown (Fig. 6) and by the transmembrane nature of the N terminus, which thus must reside at one of the two membrane contact points below the basal lobe and leg domain (Fig. 3*B*). Since the MTase-GTase core region (amino acids ~91 to 215) (Fig. 1) is directly linked to the N-terminal transmembrane segment, it must be adjacent to the membrane. These considerations imply that the N-terminal half of protein A, from the N-terminal transmembrane region, MTase-GTase core through the possibly membrane-interacting Iceberg region together comprise the entire basal region of the crown, including both membrane interaction sites and the basal lobe. While the enzymatically active RNA-capping region, including the MTase-GTase core and some flanking Iceberg sequences, might be a candidate to occupy the basal lobe, assigning specific positions for these sequence elements in the basal crown structure requires even higher imaging resolution or further mapping results.

Thus, the transmembrane-anchoring of the MTase-GTase core to the basal membrane and the C-terminusposition at the crown apex both indicate that the C-proximal RdRp must occupy the remaining apical lobe. Such RdRps share a highly conserved fold and Fig. 7 shows that the predicted flavivirus-like fold of the FHV RdRp fits well into the apical lobe with clear preference for the narrower C terminus at the top, matching the nanogold mapping, and the wider N terminus at the bottom, consistent again with the association of the full protein A N terminus with the basal membrane. The substantial binding surface between the bottom of each apical domain and the top of the underlying basal domain (Movie S4) demonstrates a strong connection between these domains but does not indicate if that binding is intra- or intermolecular. Thus, a single protein A might constitute either a vertically stacked pair of basal and apical domains or the more helical union of a basal lobe with the apical lobe to either left or right (Fig. 3*A*). Solving this intramolecular connectivity between apical and basal lobes may ultimately require resolving and tracing protein A's α-carbon backbone.

Crown–Membrane Interactions. Each crown segment interacts with the underlying membrane at two distinct sites flanking the highest curvature of the lipid bilayer (Figs. 3*B* and 8*B*). Through these contacts, the crown closely constrains the replication vesicle neck to a constant diameter and curvature that was reinforced in subtomogram averaging, despite wide variations in the diameters of the associated vesicles (Fig. 2*A*) (25). Twelvefold repetition of these membrane contacts in the crown likely is important to provide sufficient force to maintain the strong local neck curvature against the counter pressures of the highly deformed vesicle membrane and densely coiled, electrostatically repulsing dsRNA within the replication vesicle (Fig. 2 *C* and *E*) (25). In the membrane region between the two protein A–membrane contacts, the density bridging the two leaflets of the bilayer (Fig. 3*B*, asterisks) might be related to the protein A transmembrane domain (23) or to unusual strain on the membrane in this region of high curvature.

Mechanistic Implications of Polymerase Mapping to Crown Apical Lobe. RdRp positioning at the apex of the crown has mechanistic implications for steps throughout the RNA replication cycle. Such positioning appears particularly consistent with early steps in RNA replication. Recruiting the viral (+)RNA template to the OMM precedes (−)RNA synthesis and requires the protein A RdRp domain bound to its membrane binding site (39). The exposed apical RdRp domain is ideally positioned to capture the incoming template (+)RNA, particularly since it is repeated 12 times. After (+)RNA template capture, (−)RNA synthesis is required to form nodavirus replication complex vesicles (19), possibly by directing the dsRNA product into the membrane to inflate the vesicle (25). Consistent with this, RNA polymerases are strong molecular motors that can generate ≥30 pN of force (51). The dodecameric nature of the crown and dual ring of membrane interaction sites would strongly anchor the RdRp as it applies such forces to expand the vesicle.

In contrast, it is difficult to explain the role, if any, of the apical RdRp in (+)RNA synthesis. First, the dsRNA template for (+) RNA synthesis is sequestered inside the replication complex vesicle, at least 9 nm away from the RdRp at the crown apex. (+) RNA synthesis by the apical RdRp would require the dsRNA template to loop out of the vesicle and return, complicating RNA synthesis and exposing the dsRNA to recognition by IFN-stimulated and RNAi innate immune pathways, thereby defeating a major benefit of the dsRNA-protecting vesicle. Second, the membrane-linked core MTase-GTase domain for m^7G capping of progeny RNA sits between the apical RdRp and vesicle-sequestered dsRNA template. Since new (+)RNAs must be synthesized, capped, and released in that order, the product (+) RNA also would have to execute a complex, looped path within the crown interior before exiting to the cytoplasm.

These challenges suggest that RdRp activity for (+)RNA synthesis might be provided by an alternate, noncrown form of protein A with better access to the dsRNA template. Evidence for a noncrown pool of protein A in nodavirus replication complexes emerged when embedded and sectioned infected cells were

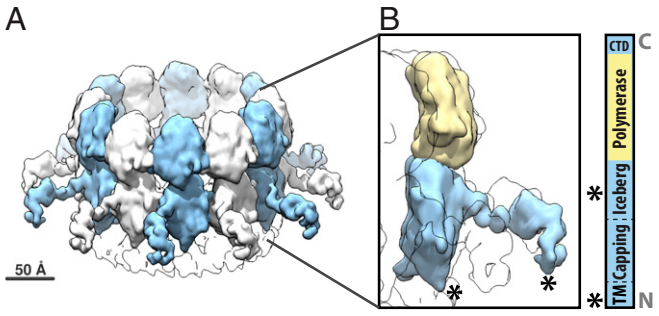

Fig. 8. Dodecameric arrangement of protein A to form the crown complex. (*A*) Tilted side view of the crown with alternate segments of the 12-fold symmetric crown colored in blue and white. The floor densities are shown in transparent white with black silhouette. (*B*) Single predicted protein A segment shown in two-color in side view with the mapped polymerase domain in yellow and remainder of protein A N-terminal densities in blue. The remaining crown segments are shown in transparent white with black silhouettes for unobstructed viewing of the highlighted crown segment. The asterisks mark the two separate membrane-interaction sites of each crown segment. A protein A linear map from the N terminus to the C terminus is shown to the right with the same color scheme as the density map. The asterisks in the protein A linear map indicate the well-characterized N-terminal transmembrane domain TM and the possible membrane-interaction domain within the Iceberg region.

immunogold-labeled with an antibody against protein A, revealing substantial labeling inside RNA replication vesicles (5). Such protein A in the replication vesicle, either at or farther inside the vesicle neck, might have functional parallels with (+)RNA synthesis by dsRNA-containing reovirus cores, where an interior RdRp copies dsRNA templates sequestered in the core, and releases nascent (+)RNAs through a crown-like pentameric ring of viral proteins that serve as an exit and RNA-capping channel (52, 53). Potentially consistent with this, top views of crowns in reconstructed tomograms often show asymmetric densities near the inside base of the crown interior (Fig. 2 *B*, *D*, and *F*). These densities might be related to long fibrils that frequently emerge from crowns, as expected for nascent progeny (+)RNA release to the cytoplasm (25), to an alternate pool of protein A, or to both. The results presented here provide strong foundations for further structural and functional studies to address these and other fundamental questions in (+)RNA virus genome replication.

Materials and Methods

Plasmids. All FHV RNA1 WT expression plasmids were derived from pIE1^{hr5}/PA backbone as described previously (19), except with one modification. The RNA1-WT plasmid was further optimized for supporting higher levels of RNA1 replication by introducing a self-cleaving hammerhead ribozyme sequence (54) upstream of the RNA1 5′UTR. To generate plasmid RNA1-GFP11-ΔB1, first the *Drosophila* codon-optimized GFP11 sequence (coding for aa RDHMVLHEYVNAAGIT*) (36), was inserted after nucleotide position 3061 (FHV RNA1 coordinates) in the expression plasmid via overlap PCR that also introduced T3034G mutation (FHV RNA1 coordinates) to change the protein A stop codon to arginine. Second, since the introduction of GFP11 sequence disrupted the FHV RNA1 3′UTR, the 3′UTR first 23 nucleotides were duplicated downstream of the GFP11 stop codon to restore the full 3′UTR sequence for optimal RNA1 replication. Finally, to knockout protein B1 expression, an A2728C mutation (FHV RNA1 coordinates) was introduced via overlap PCR to knockout B1 expression, which also introduced a M897L change in protein A ORF. To generate RNA1-His-ΔB1, the expression plasmid RNA-GFP11-ΔB1 was modified to introduce M1011H, V1012H, L1013H, and E1015H residue changes in the protein A ORF creating a His-tag. The RNA1-fs plasmid has been previously described (39). The FHV RNA2 expression plasmid (pMT-RNA2) was designed by swapping the IE1 promoter with a metallothionein (MT) promoter in a previously described plasmid pIE1^{hr5}-RNA2 (19).

GFP1-10 *Drosophila* expression plasmid (pIE1-GFP1-10) was constructed by codon optimizing the GFP1-10 nucleotide sequence (36) and synthesizing a custom DNA gBlock (Integrated DNA Technologies). The resulting gBlock sequence was PCR-amplified and cloned into the pIE1^{hr5}/PA backbone downstream of the IE1 promoter using the HindIII restriction sites.

To generate the *E. coli* expression vector for GFP1-10, pIE1-GFP1-10 was digested with EcoRV and Eco53kI and the resulting GFP1-10 fragment was inserted into an XmnI digested pMAL-c5x (New England Biolabs) vector. This plasmid, pMAL-GFP1-10, expresses GFP1-10 fused to MBP at its N terminus under the control of isfopropyl-β-D-thiogalactopyranoside (IPTG)-inducible tac promoter.

Cell Culture. *Drosophila* S2 cells were obtained from ATCC ([*Drosophila* line 2, D. Mel (2), SL2], ATCC CRL-1963) and maintained at 28 °C in Express Five serum-free medium (Gibco) supplemented with penicillin, streptomycin, amphotericin B, and L-glutamine (E0F). *Drosophila* DL-1 cells were kindly provided by Paul Friesen (University of Wisconsin–Madison, WI) and maintained at 28 °C in Schneider's *Drosophila* medium (Gibco) supplemented with 10% FBS, penicillin, streptomycin, and amphotericin B (S10F).

Infections and Mitochondrial Isolation for Tomography. Infections with wild-type FHV were performed at a multiplicity of infection (MOI) of 10, whereas the infections for FHV-His-ΔB1 were performed at an MOI of 5 on *Drosophila* S2 cells. For all infections, 10^8 cells were pelleted and resuspended in 1 mL of S10F media. Then purified virus was added at the indicated MOI and the cells were infected on a gyrating shaker at 150 rpm for 1 h. Later, 14 mL of S10F was added to the cells and transferred to a T75 flask and incubated for 16 to 18 h at 28 °C. Postincubation, the cells were harvested and high-purity mitochondria were isolated using a Qproteome mitochondrial isolation kit (Qiagen). We identified that prior mitochondrial isolation techniques led to an unanticipated ∼10 kDa protease digestion product of protein A. We systematically screened protease inhibitors to find an effective protease inhibitor mix that protects protein A against digestion throughout the various steps of high-purity mitochondrial isolation (*SI Appendix*, Fig. S1). Based on our findings, we replaced the supplier-provided protease inhibitor with Halt EDTA-free protease inhibitor (ThermoFisher). For WT FHV infections, the final mitochondrial pellets were resuspended in supplier-provided mitochondria storage buffer at A280 absorbance of 10. For FHV-His-ΔB1 infections, the final mitochondria pellet was washed gently three times and resuspended in a custom nanogold binding buffer (50 mM Hepes pH 7.2, 136 mM KCl, 2% sucrose, and 10 mM imidazole) at A280 absorbance of 10.

Immunofluorescence Imaging. Transfected or infected *Drosophila* S2 cells were used for immunofluorescence imaging. The transfection and infection procedures were as described in the section above. Cells were harvested and processed for immunofluorescence imaging as previously described (55). For protein A immunostaining, 1:500 dilution of the rabbit antiserum against protein A was used [Antibody R1194 (26)]. For His-tag immunostaining, 1:100 dilution of mouse monoclonal, clone H8, antibody (ab18184, Abcam) was used. Widefield epifluorescence microscopy was performed on the Nikon Ti microscope and the images were acquired using NIS-Elements software (Nikon). Additional image processing was done using the Fiji (ImageJ) software package (56). PCC were calculated using the EzColocalization plugin for ImageJ (57) where, −1 = complete anticolocalization, 0 = noncolocalization, and 1 = complete colocalization.

Plunge-Freezing and Screening. For plunge-freezing and screening, 200-mesh Quantifoil cryogrids (2/2) (Cat: Q2100CR2, Electron Microscopy Sciences) were glow-discharged for 60 s using PELCO easiGlow (Ted Pella). Three microliters of mitochondrial preparations mixed 1:1 by volume with 10 nm BSA Gold Tracer (Electron Microscopy Sciences) were applied on the cryogrid. The cryogrids were vitrified in liquid ethane using a Vitrobot (FEI, ThermoFisher) under 100% humidity and 22 °C in the blotting chamber. The freezing parameters was set as follows: 1) forceps offset 0, 2) waiting time 2 s, 3) blotting time2 s, 4) drain time 10 s. For screening the quality of ice and sample density, the vitrified cryogrids were inspected with an TF30 transmission electron microscope (FEI, ThermoFisher) equipped with a field emission gun operated at 300 kV, a postcolumn energy filter (Gatan), and a Gatan K2 summit direct electron detector.

Imaging Acquisition for Cryotomography. The dataset to generate the 8.5-Å crown subtomogram average was acquired at the Pacific Northwest Cryo-EM Center (Portland, OR) facility. For this dataset, the vitrified cryogrids were placed in the cartridges of autoloader that were loaded into a Titan Krios (Thermo Fisher Scientific) operated at liquid nitrogen temperature, equipped with a field-emission gun operated at 300 kV, a postcolumn energy filter (Gatan) operated at zero-loss, and a Bioquantum K3 direct electron detector with a 5,760 × 4,092-pixel sensor (Gatan). After low-magnification 100× full-grid montages were collected, an intermediate magnification montages of areas with thinner vitrified ice and abundant samples were collected at 2,000×. Subsequently, the region of interests were picked from the intermediate montages for a tilt-series collection. Tilt-series were collected from −54° to +54° or −60° to +60°, respectively, by 3° increments at a defocus of −3.5 μm using a grouped dose-symmetric tilt scheme (30) starting from 0° at a dose rate set at 15 e-/unbinned pixel per second. The accumulated dose for the entire tilt-series was 180 $e^-/Å^2$, and the accumulated dose for each tilt was at 4.86 $e^-/Å^2$ and 4.39 $e^-/Å^2$ and total exposure/tilt was 0.67 and 0.6 s for the −54° to +54° and −60° to +60° tilt range, respectively. Each tilt was fractionated to 20 frames at superresolution mode on the Bioquantum K3 at pixel size 1.078 Å per pixel.

Cryotomograms for His-tagged FHV infected mitochondrial samples were collected with a Titan Krios (ThermoFisher) at the Janelia Farms Research Campus (Howard Hughes Medical Institute) equipped with a postcolumn energy filter (GIF) and a K2 summit direct electron detector. Tilt-series were collected from −60° to +60° by 3° increments at a defocus of −3.5 μm using a dose-symmetric tilt scheme (30) starting from 0° at a dose rate set at 8 e^-/unbinned pixel per second. The accumulated dose for the entire tilt-series was 180 $e^-/Å^2$, and the accumulated dose for each tilt was at 4.39 $e^-/Å^2$. The exposure time was set to 3.7 s and each tilt was fractionated to 10 frames at super resolution mode on the K2 summit at pixel size 1.35 Å per pixel.

Imaging Processing. Individual tilt-containing frames were transferred to the University of Wisconsin–Madison Center for High-Throughout Computing (CHTC) platform located at the University of Wisconsin–Madison and the frames were processed to correct drift by using MotionCor2, v1.2.0 (29). The CTF estimation for each tilt was performed by using emClarity 1.4.3 (34), and the particles were selected by using automatic template search function

within emClarity using a 24 Å initial averaged model generated from 1,608 crowns from 27 tomograms by IMOD/PEET (32). Subsequent 3D CTF correction, tomogram reconstruction, and subtomogram averaging were performed using emClarity on the SLURM-based server of the Pacific Northwest National Laboratory.

For His-tag mapping by using Ni-NTA-nanogold, individual sets of frames from the tilt-series were uploaded to the CHTC platform and the frames were processed to correct drift by using the Unblur v1.02 algorithm within the software suite CisTEM v1.0.0 (58). The CTF correction for each tilt-series was performed by using CTFPhaseflip function and the tomograms were generated by using Etomo/IMOD software v4.9.12 (59) on a local workstation (Dell). Particles were picked from each tomogram manually using IMOD and orientations of the crowns were defined by using the StalkInit function in PEET/IMOD (32, 33). Subtomogram averaging was performed using PEET/IMOD on a local workstation.

All image rendering on subtomogram-averaging density maps were performed using Chimera (University of California, San Francisco) (60) and IMOD. Density-map segmentation and rigid-body docking was performed using "Segment Map" and "Fit to Segment" Chimera plugins within the software suite Segger v1.9.5 (46, 47).

Additional methods are provided in the *SI Appendix, Supplementary Methods*.

Data Availability. An electron-density map of the nodaviral replication protein A crown complex has been deposited in the EMDataBank, https://www.ebi.ac.uk/pdbe/emdb/, under accession code EMD-22129 (61).

ACKNOWLEDGMENTS. We thank Zhiheng Yu, Rick Huang, Xiaowei Zhao, and Doreen Matthies at the HHMI Janelia Cryo-EM Facility for help in microscope operation and data collection; Alex Kvit for constant support with the Tecnai TF30 cryotomography sample screening and data collection; Jean-Yves Sgro for assistance with University of California, San Francisco-Chimera; and Claudia Lopez, Lauren Hales-Beck, Craig Yoshioka, and Harry Scott of the Pacific Northwest Cryo-EM Center for assistance with scheduling, sample preparation, and data collection. A portion of this research was supported by NIH Grant U24GM129547 and performed at the Pacific Northwest Cryo-EM Center at Oregon Health and Sciences University and accessed through EMSL (grid.436923.9), a Department of Energy Office of Science User Facility sponsored by the Office of Biological and Environmental Research. This research was performed using the compute resources and assistance of the University of Wisconsin–Madison Center for High-Throughput Computing (CHTC) in the Department of Computer Sciences. The CHTC is supported by University of Wisconsin–Madison, the Advanced Computing Initiative, the Wisconsin Alumni Research Foundation, the Wisconsin Institutes for Discovery, and the NSF, and is an active member of the Open Science Grid, which is supported by the NSF and the US Department of Energy's Office of Science. P.A. is an investigator of the HHMI and the Morgridge Institute for Research and gratefully acknowledges support from these institutes, the NIH, and the John W. and Jeanne M. Rowe Center for Research in Virology.

1. J. A. den Boon, A. Diaz, P. Ahlquist, Cytoplasmic viral replication complexes. *Cell Host Microbe* **8**, 77–85 (2010).
2. C. Harak, V. Lohmann, Ultrastructure of the replication sites of positive-strand RNA viruses. *Virology* **479–480**, 418–433 (2015).
3. H. J. Maier *et al*., Extensive coronavirus-induced membrane rearrangements are not a determinant of pathogenicity. *Sci. Rep.* **6**, 27126 (2016).
4. K. Knoops *et al*., SARS-coronavirus replication is supported by a reticulovesicular network of modified endoplasmic reticulum. *PLoS Biol.* **6**, e226 (2008).
5. B. G. Kopek, G. Perkins, D. J. Miller, M. H. Ellisman, P. Ahlquist, Three-dimensional analysis of a viral RNA replication complex reveals a virus-induced mini-organelle. *PLoS Biol.* **5**, e220 (2007).
6. I. Romero-Brey *et al*., Three-dimensional architecture and biogenesis of membrane structures associated with hepatitis C virus replication. *PLoS Pathog.* **8**, e1003056 (2012).
7. S. Welsch *et al*., Composition and three-dimensional architecture of the dengue virus replication and assembly sites. *Cell Host Microbe* **5**, 365–375 (2009).
8. W. C. Brown *et al*., Extended surface for membrane association in Zika virus NS1 structure. *Nat. Struct. Mol. Biol.* **23**, 865–867 (2016).
9. R. N. Kirchdoerfer, A. B. Ward, Structure of the SARS-CoV nsp12 polymerase bound to nsp7 and nsp8 co-factors. *Nat. Commun.* **10**, 2342 (2019).
10. M. Gu, C. M. Rice, Structures of hepatitis C virus nonstructural proteins required for replicase assembly and function. *Curr. Opin. Virol.* **3**, 129–136 (2013).
11. W. Hao *et al*., Crystal structure of Middle East respiratory syndrome coronavirus helicase. *PLoS Pathog.* **13**, e1006474 (2017).
12. Y. S. Law *et al*., Structural insights into RNA recognition by the Chikungunya virus nsP2 helicase. *Proc. Natl. Acad. Sci. U.S.A.* **116**, 9558–9567 (2019).
13. G. Lu, P. Gong, Crystal structure of the full-length Japanese encephalitis virus NS5 reveals a conserved methyltransferase-polymerase interface. *PLoS Pathog.* **9**, e1003549 (2013).
14. S. Ricagno *et al*., Crystal structure and mechanistic determinants of SARS coronavirus nonstructural protein 15 define an endoribonuclease family. *Proc. Natl. Acad. Sci. U.S.A.* **103**, 11892–11897 (2006).
15. D. Su *et al*., Dodecamer structure of severe acute respiratory syndrome coronavirus nonstructural protein nsp10. *J. Virol.* **80**, 7902–7908 (2006).
16. Y. Zhao *et al*., A crystal structure of the dengue virus NS5 protein reveals a novel interdomain interface essential for protein flexibility and virus replication. *PLoS Pathog.* **11**, e1004682 (2015).
17. M. Nishikiori *et al*., Crystal structure of the superfamily 1 helicase from Tomato mosaic virus. *J. Virol.* **86**, 7565–7576 (2012).
18. P. A. Venter, A. Schneemann, Recent insights into the biology and biomedical applications of flock house virus. *Cell. Mol. Life Sci.* **65**, 2675–2687 (2008).
19. B. G. Kopek, E. W. Settles, P. D. Friesen, P. Ahlquist, Nodavirus-induced membrane rearrangement in replication complex assembly requires replicase protein A, RNA templates, and polymerase activity. *J. Virol.* **84**, 12492–12503 (2010).
20. T. Ahola, D. G. Karlin, Sequence analysis reveals a conserved extension in the capping enzyme of the alphavirus supergroup, and a homologous domain in nodaviruses. *Biol. Direct* **10**, 16 (2015).
21. L. A. Ball, Requirements for the self-directed replication of flock house virus RNA 1. *J. Virol.* **69**, 720–727 (1995).
22. T. Quirin, Y. Chen, M. K. Pietilä, D. Guo, T. Ahola, The RNA capping enzyme domain in protein A is essential for flock house virus replication. *Viruses* **10**, 483 (2018).
23. D. J. Miller, P. Ahlquist, Flock house virus RNA polymerase is a transmembrane protein with amino-terminal sequences sufficient for mitochondrial localization and membrane insertion. *J. Virol.* **76**, 9856–9867 (2002).
24. B. T. Dye, D. J. Miller, P. Ahlquist, In vivo self-interaction of nodavirus RNA replicase protein a revealed by fluorescence resonance energy transfer. *J. Virol.* **79**, 8909–8919 (2005).
25. K. J. Ertel *et al*., Cryo-electron tomography reveals novel features of a viral RNA replication compartment. *eLife* **6**, e25940 (2017).
26. D. J. Miller, M. D. Schwartz, P. Ahlquist, Flock house virus RNA replicates on outer mitochondrial membranes in Drosophila cells. *J. Virol.* **75**, 11664–11676 (2001).
27. M. Kudryashev, D. Castaño-Díez, H. Stahlberg, Limiting factors in single particle cryo electron tomography. *Comput. Struct. Biotechnol. J.* **1**, e201207002 (2012).
28. C. E. Melia, T. A. M. Bharat, Locating macromolecules and determining structures inside bacterial cells using electron cryotomography. *Biochim. Biophys. Acta. Proteins Proteomics* **1866**, 973–981 (2018).
29. S. Q. Zheng *et al*., MotionCor2: Anisotropic correction of beam-induced motion for improved cryo-electron microscopy. *Nat. Methods* **14**, 331–332 (2017).
30. W. J. H. Hagen, W. Wan, J. A. G. Briggs, Implementation of a cryo-electron tomography tilt-scheme optimized for high resolution subtomogram averaging. *J. Struct. Biol.* **197**, 191–198 (2017).
31. B. Turoňová, F. K. M. Schur, W. Wan, J. A. G. Briggs, Efficient 3D-CTF correction for cryo-electron tomography using NovaCTF improves subtomogram averaging resolution to 3.4 Å. *J. Struct. Biol.* **199**, 187–195 (2017).
32. J. M. Heumann, A. Hoenger, D. N. Mastronarde, Clustering and variance maps for cryo-electron tomography using wedge-masked differences. *J. Struct. Biol.* **175**, 288–299 (2011).
33. D. Nicastro *et al*., The molecular architecture of axonemes revealed by cryoelectron tomography. *Science* **313**, 944–948 (2006).
34. B. A. Himes, P. Zhang, emClarity: Software for high-resolution cryo-electron tomography and subtomogram averaging. *Nat. Methods* **15**, 955–961 (2018).
35. S. Moradi, A. Nowroozi, M. Shahlaei, Shedding light on the structural properties of lipid bilayers using molecular dynamics simulation: A review study. *RSC Adv.* **9**, 4644–4658 (2019).
36. S. Cabantous, T. C. Terwilliger, G. S. Waldo, Protein tagging and detection with engineered self-assembling fragments of green fluorescent protein. *Nat. Biotechnol.* **23**, 102–107 (2005).
37. H. Li, W. X. Li, S. W. Ding, Induction and suppression of RNA silencing by an animal virus. *Science* **296**, 1319–1321 (2002).
38. T. A. Harper, "Characterization of the proteins encoded from the nodaviral subgenomic RNA," PhD thesis, University of Wisconsin–Madison, Madison, WI (1994).
39. P. M. Van Wynsberghe, H.-R. Chen, P. Ahlquist, Nodavirus RNA replication protein a induces membrane association of genomic RNA. *J. Virol.* **81**, 4633–4644 (2007).
40. C. J. Ackerson, R. D. Powell, J. F. Hainfeld, Site-specific biomolecule labeling with gold clusters. *Methods Enzymol.* **481**, 195–230 (2010).
41. J. W. Chang *et al*., Hybrid electron microscopy-FRET imaging localizes the dynamical C-terminus of Tfg2 in RNA polymerase II-TFIIF with nanometer precision. *J. Struct. Biol.* **184**, 52–62 (2013).
42. M. Meury *et al*., Detergent-induced stabilization and improved 3D map of the human heteromeric amino acid transporter 4F2hc-LAT2. *PLoS One* **9**, e109882 (2014).
43. V. Reddy, E. Lymar, M. Hu, J. F. Hainfeld, 5 nm gold-Ni-NTA binds His tags. *Microsc. Microanal.* **11**, 1118–1119 (2005).
44. S. Venkataraman, B. V. L. S. Prasad, R. Selvarajan, RNA dependent RNA polymerases: Insights from structure, function and evolution. *Viruses* **10**, 76 (2018).
45. J. Yang *et al*., The I-TASSER suite: Protein structure and function prediction. *Nat. Methods* **12**, 7–8 (2015).
46. G. D. Pintilie, J. Zhang, T. D. Goddard, W. Chiu, D. C. Gossard, Quantitative analysis of cryo-EM density map segmentation by watershed and scale-space filtering, and fitting of structures by alignment to regions. *J. Struct. Biol.* **170**, 427–438 (2010).

47. G. Pintilie, W. Chiu, Comparison of Segger and other methods for segmentation and rigid-body docking of molecular components in cryo-EM density maps. *Biopolymers* **97**, 742–760 (2012).
48. M. L. Quillin, B. W. Matthews, Accurate calculation of the density of proteins. *Acta Crystallogr. D Biol. Crystallogr.* **56**, 791–794 (2000).
49. J. Tsai, R. Taylor, C. Chothia, M. Gerstein, The packing density in proteins: Standard radii and volumes. *J. Mol. Biol.* **290**, 253–266 (1999).
50. P. J. Fleming, F. M. Richards, Protein packing: Dependence on protein size, secondary structure and amino acid composition. *J. Mol. Biol.* **299**, 487–498 (2000).
51. H.-Y. Wang, T. Elston, A. Mogilner, G. Oster, Force generation in RNA polymerase. *Biophys. J.* **74**, 1186–1202 (1998).
52. X. Zhang *et al*., In situ structures of the segmented genome and RNA polymerase complex inside a dsRNA virus. *Nature* **527**, 531–534 (2015).
53. X. Wang *et al*., Structure of RNA polymerase complex and genome within a dsRNA virus provides insights into the mechanisms of transcription and assembly. *Proc. Natl. Acad. Sci. U.S.A.* **115**, 7344–7349 (2018).
54. A. C. Forster, R. H. Symons, Self-cleavage of virusoid RNA is performed by the proposed 55-nucleotide active site. *Cell* **50**, 9–16 (1987).
55. N. Unchwaniwala, N. M. Sherer, D. D. Loeb, B. Hepatitis, Hepatitis B virus polymerase localizes to the mitochondria, and its terminal protein domain contains the mitochondrial targeting signal. *J. Virol.* **90**, 8705–8719 (2016).
56. J. Schindelin *et al*., Fiji: An open-source platform for biological-image analysis. *Nat. Methods* **9**, 676–682 (2012).
57. W. Stauffer, H. Sheng, H. N. Lim, EzColocalization: An ImageJ plugin for visualizing and measuring colocalization in cells and organisms. *Sci. Rep.* **8**, 15764 (2018).
58. T. Grant, A. Rohou, N. Grigorieff, *cis*TEM, user-friendly software for single-particle image processing. *eLife* **7**, e35383 (2018).
59. D. N. Mastronarde, S. R. Held, Automated tilt series alignment and tomographic reconstruction in IMOD. *J. Struct. Biol.* **197**, 102–113 (2017).
60. E. F. Pettersen *et al*., UCSF Chimera—A visualization system for exploratory research and analysis. *J. Comput. Chem.* **25**, 1605–1612 (2004).
61. N. Unchwaniwala *et al*, Nodavirus RNA replication complex crown. The Electron Microscopy Data Bank. https://www.emdataresource.org/EMD-22129. Deposited 8 June 2020.